Spatial variations in membrane properties in the intact rat lens

G. J. Baldo and R. T. Mathias
Department of Physiology & Biophysics, The State University of New York at Stony Brook, Stony Brook, New York 11794-8661 USA

ABSTRACT We have used linear frequency domain techniques to measure impedance at various locations and depths in the intact rat lens. The data are used to obtain best-fit solutions to a new electrical model based on lens structure, allowing us to estimate localized conductances of surface cell membranes (G_s), fiber cell membranes (g_m), and gap junctions (G_j) as functions of position. We find that g_m is small and fairly uniform throughout the lens (2.02 ± 0.58 $\mu S/cm^2$); for the anterior surface epithelial cells G_s = 1.26 ± 0.19 mS/cm^2; for the posterior surface differentiating fiber cells G_s = 0.46 ± 0.04 mS/cm^2. Thus, G_s varies about the equator in a stepwise fashion. G_j between fiber cells at locations interior to 80% of the radius is fairly uniform (0.75 S/cm^2); but in the outer 20% G_j varies smoothly and symmetrically from both poles (0.66 S/cm^2) to equator (5.95 S/cm^2). This pattern of variation in G_j is similar to the pattern of inward and outward currents reported by Robinson and Patterson (1983. *Curr. Eye Res.* 2:843–847). We therefore suggest that the nonuniform distribution of functional gap junctions, not the surface cell conductance or Na/K pumps, may be responsible for directing these current flows. Gap junctional uncoupling during exposure to elevated calcium and acidification was also examined. High calcium (20 mM, with the calcium ionophore A23187) produced modest (twofold) irreversible uncoupling along with large, irreversible decreases in membrane potential. We did not pursue this further. Acidification with 20 and 100% CO_2-bubbled Tyrode's produced 5- and 15-fold reversible uncoupling, respectively, only in the outer 20% of the lens radius. The remaining inner 80% of the lens gap junctions seemed resistant to the acidification and did not uncouple.

INTRODUCTION

The lens is a syncytial structure consisting primarily of tightly packed, elongated fiber cells oriented from pole to pole and interconnected by gap junctions. The inner, mature fiber cells are almost completely devoid of organelles but contain a large amount of the crystallin proteins that aid in focusing light. The anterior hemisphere is capped by a single layer of epithelial cells which actively transport sodium and potassium. In keeping with its light-passing function, the lens is devoid of any vascularization that might otherwise obstruct the light path. How the inner fiber cells maintain their transmembrane ion gradients and remain healthy is an intriguing question, since (*i*) they do not contain the mitochondria required for ATP production, and (*ii*) their tight packing creates restricted extracellular spaces which pose a substantial barrier to free diffusion of glucose and metabolites (see review by Mathias and Rae, 1989). For example, given an average rat lens diameter of 0.38 cm and a diffusion coefficient on the order of 10^{-6} cm^2/s, >1.5 h would be required for a solute particle to traverse the distance between the periphery and the center of the lens.

Clearly the perfusion of the inner fiber cells by free diffusion alone is minimal and an additional circulatory mechanism may be required, as suggested by Mathias and Rae (1985). Other evidence for this hypothetical mechanism comes from the work of Robinson and Patterson (1983) and Parmelee et al. (1985) using the vibrating probe. They have measured regionalized outward currents at the lens equator and inward currents at both poles. It is possible that these localized currents produce osmotic gradients that drive water and solute flux through the lens, thus providing an avascular circulation. The source of these gradients may ultimately be the Na/K pumps located in the surface cells of the lens, but the factors directing the currents are not well understood.

Using linear frequency-domain impedance techniques (Mathias et al., 1981), we have obtained best-fit parameter values for a new equivalent circuit model that allows for angular (pole to pole) variations in surface cell membrane conductance, and both angular and radial (center to periphery) variations in effective intracellular resistivity. We find a smooth, symmetric dependence about the equator of gap junctional coupling between peripheral fiber cells, and an anterior to posterior, steplike dependence of surface cell membrane conductance in the rat lens. The difference in the angular dependencies of these two parameters suggests that the nonuniform distribution of gap junctions may be responsible for directing the current flows reported by Robinson and Patterson (1983), instead of the surface cell conductance or Na/K pumps.

We have also examined the uncoupling of gap junctions after acidification and exposure to high calcium. These studies, like previous studies in the frog lens (Mathias et al., 1991), suggest that the gap junctional proteins connecting the inner fiber cells have lost their pH sensitivity, whereas those connecting the peripheral cells uncouple when the cytoplasm is acidified. Since the outer fiber cells are continually pressed inward, becoming inner fiber cells during the normal maturation of the lens, the properties of the gap junctional proteins are apparently modified with age.

0006-3495/92/08/518/12 $2.00

METHODS

Sprague-Dawley rats (50–75 g, lens radius of 1.65–1.9 mm) of either sex were euthanized and both eyes enucleated and placed in a beaker containing Tyrode's solution. For the actual lens dissection, eyes were placed in a petri dish half filled with sylgard. A hemispherical depression in the center of the sylgard provided a means of support during dissection. The cornea and iris were removed to expose the anterior portion of the lens, the eye was inverted, and the sclera was quartered from optic nerve to zonules. This created four flaps which were used to pin the lens to the bottom of the experimental chamber.

Normal Tyrode's solution was made using Tyrode's salts (cat. #T2145; Sigma Chemical Co., St. Louis, MO) supplemented with 1.2 mM KCl and 5 mM HEPES. This gave overall concentrations of (mM): 149.3 Na^+, 3.5 K^+, 145.5 Cl^-, 12 HCO_3^-, 0.3 PO_3^{-2}, 1.8 Ca^{+2}, 0.5 Mg^{2+}, 5.5 glucose, and 5 HEPES, titrated to pH 7.4 using NaOH. The 20 mM Ca^{2+} solution contained (mM): 110 Na^+, 4.1 K^+, 155 Cl^-, 20 Ca^{2+}, 0.5 Mg^{2+}, 5.5 glucose, and 5 HEPES. In addition, 1 μM of the calcium ionophore A23187, dissolved in DMSO, was added to allow Ca^{2+} to cross cell membranes.

Glass microelectrodes were pulled on a Flaming Brown model P80/PC puller (Sutter Instrument Co., San Rafael, CA), using 1.5-mm-diam glass capillary tubes, and back-filled with 2.5 M potassium acetate solution. DC resistances ranged between 5 and 10 MΩ. Indifferent bath electrodes were made by breaking the tips of empty glass electrodes and filling them with a warmed agar solution containing 0.2 g of agar powder dissolved in 20 ml of 2.5 M potassium acetate.

Lenses were pinned by their scleral flaps into the sylgard bottom of a lucite experimental chamber, which was temperature controlled at 35°C, and continuously perfused with Tyrode's solution. White noise current was passed into the lens through a microelectrode positioned as near the center of the lens as possible. The voltage induced by this current was recorded by a second microelectrode placed at whatever depth and location was required for a particular experiment. The circuits used to record voltage and current are described in Mathias et al., (1981). The injected intracellular current and the induced intracellular voltage were fed to the inputs of a model 5420 Fourier analyzer (Hewlett-Packard Co., Palo Alto, CA), which is capable of collecting and averaging impedance data in real time. Usually 50–100 impedance curves from the same location at a given bandwidth were averaged for incorporation into the final data set; the averaged data were then stored on an IBM PC for subsequent curvefitting, as described in Mathias et al. (1991), and analyzed using the model described here.

In actuality, it was necessary to record the frequency band between 0.08 and 800 Hz in three separate segments to obtain the desired low frequency resolution. High frequency cutoffs at 12, 100, and 800 Hz were chosen for this purpose. The computer was used to merge the three segments into one continuous set and edit out spurious points (usually the odd harmonics of the 60-Hz line frequency). Finally, the merged impedance magnitude and phase angle data were fit by the computer to an equivalent circuit model using a least-squares method described in Mathias et al. (1981).

GLOSSARY

a	lens radius (cm)
α	$\alpha\bar{R}_i$ is the value of $R_{i,r}$ for $0 \le r \le r_0$ (unitless)
β_e	$R_{e,r}/R_{e,a}$ (unitless)
β_i	$\alpha\bar{R}_i/R_{i,a}$ (unitless)
c_m	inner fiber cell membrane capacitance (F/cm^2)
C_s	surface cell capacitance (F/cm^2)
G_a	surface cell conductance of anterior hemisphere (S/cm^2)
g_m	inner fiber cell membrane conductance (S/cm^2)
G_{min}	mean deviation from 0 of $g(\theta)$ between 0 and $\bar{\theta}$
G_{max}	mean deviation from 0 of $g(\theta)$ between $\bar{\theta}$ and $\pi/2$
G_p	surface cell conductance of posterior hemisphere (S/cm^2)
$G_s(\theta)$	surface cell conductance; see Eq. 1 (S/cm^2)
$g(\theta)$	an angular conductivity function for $R_{i,r}$ in the outer shell (see Eqs. 2 and 3)
$I(j\omega)$	current injected into lens (A)
$i_e(r, \theta, j\omega)$	extracellular current density (A/cm^2)
$i_i(r, \theta, j\omega)$	intracellular current density (A/cm^2)
$P_n(\cos\theta)$	Legendre polynomial (unitless)
$\psi(r, \theta)$	induced lens voltage under conditions where $\psi_i \to \psi_e = \psi$ (V)
$\psi_e(r, \theta, j\omega)$	extracellular potential (V)
$\psi_i(r, \theta, j\omega)$	intracellular potential (V)
r	radial distance from lens center (cm)
r_0	radial distance to the lens outer shell, which contains the angular variations (cm)
$R_{e,r}$	effective radial extracellular resistivity (Ω-cm)
$R_{e,a}$	effective angular extracellular resistivity (Ω-cm)
$\bar{R}_i$	average effective radial intracellular resistivity in the outer shell; see Eq. 2 (Ω-cm)
$R_{i,r}(r, \theta)$	effective radial intracellular resistivity (Ω-cm)
$R_{i,a}$	effective angular intracellular resistivity (Ω-cm)
$R_s(r, \theta)$	high frequency resistance between r and a; see Eq. A30 (Ω)
S_m/V_t	surface area of all cell membranes per unit volume of tissue (cm^{-1})
θ	angular location coordinate (degrees or radians, 0° = posterior pole)
$\bar{\theta}$	angular location where $g(\bar{\theta}) = 0$
$Z_L(r, \theta, j\omega)$	lens input impedance (Ω)

THEORETICAL DEVELOPMENT OF THE ANGULAR LENS MODEL

Our analysis of the lens is based primarily on its anatomical structure, as described in the Introduction and illustrated in Fig. 1 *A*. We treat the lens as being symmetric about an axis passing through the poles, with electrical properties that may vary as functions of angular location, θ, where $\theta = 0°$ is defined as the posterior pole, and radial location, r, where $r = 0$ is defined as the lens center. Fig. 1 *B* illustrates the equivalent circuit used to represent this arrangement. A current (I) passed via an intracellular microelectrode at the lens center induces a voltage ψ_i that depends on θ and r. This current is shunted to the extracellular space across the fiber cell membrane conductance (g_m, S/cm^2) and capacitance (c_m, F/cm^2). Radially flowing intracellular current crosses gap junctions approximately every 3 μm (the cell thickness), whereas angularly flowing current moves hundreds of microns along the axis of fiber cells before crossing gap junctions. As a result, the effective intracellular resistivity in the radial direction, $R_{i,r}$ (Ω-cm) is much higher than in the angular direction ($R_{i,a}$, Ω-cm).

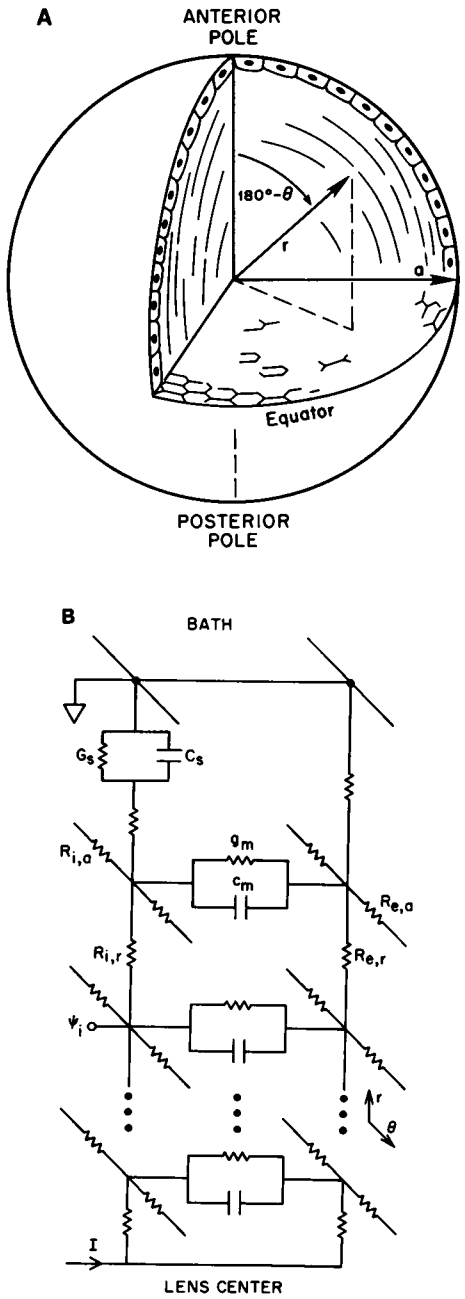

FIGURE 1 Anatomical and equivalent circuit model of the lens. (*A*) Major features of the lens include the epithelial cell layer capping the anterior hemisphere and the pole to pole orientation of the fiber cells. We define the lens radius to be a, and the angular location, θ, as 0° at the posterior pole. The radial position of the voltage electrode, r, is defined as the distance from the center of the lens. (*B*) White noise current (I) injected intracellularly near the center of the lens flows from fiber cell to fiber cell through gap junctions ($R_{i,r}$) to the surface cell membranes where it flows across G_s and C_s into the bath. Alternatively, the current can flow across a fiber cell membrane through g_m and c_m to the restricted extracellular space ($R_{e,r}$) into the bath. Intracellular current can also flow angularly along the axis of the fiber cells ($R_{i,a}$) and extracellular current can circulate in the θ direction along $R_{e,a}$. The voltage induced by the current (ψ_i) can be measured at any location (r, θ) by suitable positioning of the voltage-recording electrode.

The effective extracellular resistivity depends on the volume fraction and tortuosity of the extracellular space. Since the tortuosity is greater in the radial direction, the effective extracellular radial resistivity, $R_{e,r}$ (Ω-cm), is greater than the angular resistivity ($R_{e,a}$, Ω-cm). Cells at the surface of the lens ($r = a$, the lens radius) are assumed to have a membrane conductance G_s (S/cm^2), which varies from anterior to posterior, and a membrane capacitance C_s (F/cm^2).

This distributed network gives rise to partial differential equations describing the intracellular and extracellular voltages (ψ_i and ψ_e, respectively, in volts) produced by an injected current. These equations have been previously solved for the case where there is no angular dependence, and describe adequately the impedance of the frog lens (Mathias et al., 1979, 1981, 1991). In this study we record the impedance of the rat lens at angular locations θ = 0°, 45°, 90°, 135°, and 180°. Although the impedance could be fit by the original model (Eisenberg et al., 1979; Mathias et al., 1981) we found that the average best-fit values of G_s and R_i varied systematically with θ (Fig. 2).

Because of the methods used to measure impedance and the derivation of the old model, these variations could produce substantial errors in our estimation of the electrical properties of the lens, and we were therefore prompted to develop a new model. The source of these errors is as follows. A current-passing microelectrode is positioned in a cell near the center of the lens and the induced intracellular voltage is recorded in a cell just below the surface ($r \approx 0.9a$). The applied current and induced voltage are used to calculate the impedance, Z_L, essentially via Ohm's law: $Z_L(r, \theta, j\omega) = \psi(r, \theta, j\omega)/I(j\omega)$. The old model assumes that this current flow is radially symmetric and uniform throughout the lens. As a result, the angular variations in G_s and R_i, shown in Fig. 2, will be underestimated, since the actual current density will be highest where resistance is lowest, and vice versa. This has the effect of smoothing the variations. The following is a rather heuristic description of the development of a new model to include these variations. A more rigorous mathematical explanation is contained in the Appendix.

Angular variation of parameters is assumed to occur near the lens surface

The analysis of the equations was simplified by locating all of the angularly dependent parameters in an outer shell or boundary layer at the lens surface. Our justification for making this assumption is as follows. Mathias et al. (1991) showed that the value of $R_{i,r}$ is determined from the high frequency asymptote of the impedance magnitude. In this limit the membrane capacitances c_m

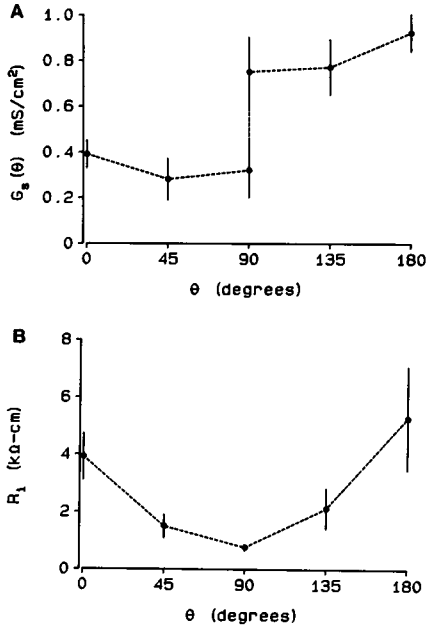

FIGURE 2 Angular variation in G_s and R_i from the old model. We fit all of our data using the angularly symmetric model of the lens described in Mathias et al. (1981). The parameter values thus determined showed: (*A*) pole to pole variation in G_s with stepwise change at equator, and (*B*) symmetric pole to equator variation in $R_{i,r}$. These observations suggested both a discontinuous surface conductance and a nonuniform distribution of gap junctional conductance (inferred from $R_{i,r}$), prompting the development of the angular model. Each point represents the average of values from four to nine lenses; error bars indicate standard deviations.

and C_s behave like short circuits and, as can be seen in Fig. 1 *B*, the induced voltage ψ depends on the current density times the parallel resistivity term $R_{i,r}R_{e,r}/(R_{i,r}+R_{e,r})$ and the distance between the point of recording and the bath. Since $R_{e,r}$ is more than an order of magnitude greater than $R_{i,r}$, the parallel sum is roughly equal to $R_{i,r}$. This means the angular dependence observed in ψ should result from a similar dependence in $R_{i,r}$.

Surprisingly, when we initially analyzed the induced voltage using the assumption that $R_{i,r}$ was a function of θ only and did not depend on r, no angular dependence in ψ was observed. An explanation for this apparent contradiction is shown in Fig. 3 *A*, where we consider the lens as having only two parallel resistance paths for injected current to flow intracellularly from the center. In the upper diagram, $R_1 \neq R_2$, but the resistivity of each is constant over distance (i.e., there is no radial dependence). Therefore, the voltage drops in each resistor are the same and at any point x, $\psi_1(x) = \psi_2(x)$. Since the two potentials are equal at any x, there is no potential difference between the resistors and, if lateral connection were made, no current would flow between them (analogous to zero current in the angular direction θ). The lower diagram of Fig. 3 *A* illustrates how angular dependence of potential can result by imposing a radial dependence on the resistivities. Resistors R in both paths are equal, but terminate on two unequal resistors, R_1 and R_2. Since the voltage drop across R_1 does not equal the drop across R_2, a voltage difference will exist in the angu-

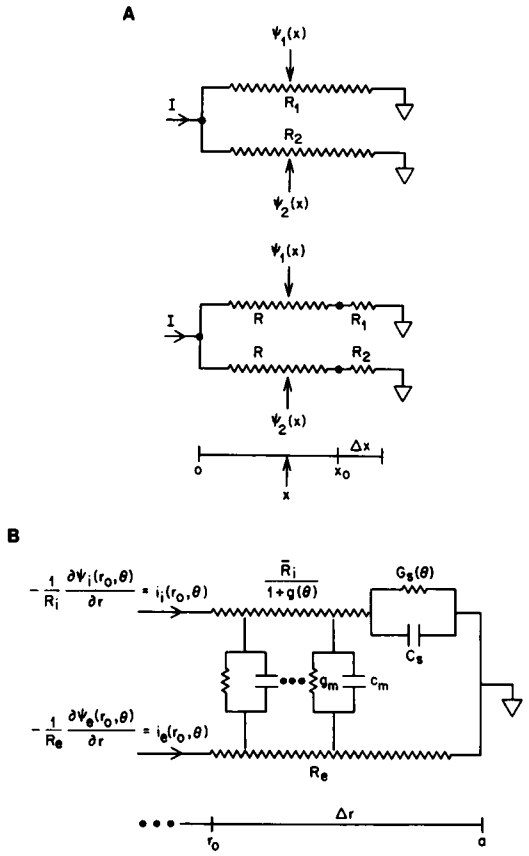

FIGURE 3 Motivation for lumping angularly dependent parameters into an outer shell. (*A*) An example of how an outer shell can produce angular variations in an inner, nonangularly varying nucleus. The upper diagram illustrates an analogue of the nonradially dependent model, having two parallel resistors of unequal resistance; R_1 and R_2, however, are constant over all x. In this situation, at any x, $\psi_1(x) = \psi_2(x)$ and no current would flow along a path connecting the resistors (i.e., the analogue of the angular direction). The lower diagram illustrates the effect of a radial change in resistance that is different in an outer shell connected to an inner region of equal parallel resistances R. Since R_1 does not equal R_2, the voltage drop at any $x < x_0$ in path 1 (ψ_1) will not be equal to the voltage drop at the same x in path 2 (ψ_2), even though the inner resistances are equal. This potential difference between the paths would create a current flow in a path connecting the resistors. (*B*) Circuit showing application of the above situation to an angular model of the lens. We assume that the angular dependence of $R_{i,r}(\theta)$ occurs only in an outer shell of thickness $a - r_0$. Note that $R_{i,r}$ includes a $g(\theta)$ term, which represents the angular dependence of the gap junctional conductance. To simplify our mathematical analysis, we ignore angular current flow in this thin shell. However, angular variation in the parameters of the shell set angularly dependent boundary conditions on the current and voltage at $r = r_0$; hence there will be angularly circulating currents throughout the lens at $r \leq r_0$.

lar direction at x_0. More importantly, the difference in voltage drop will also produce a difference in potential at any point x between path 1 and path 2, even though the inner resistivities are equal. Thus, a thin outer shell of unequal resistances can result in an angular current flow at all radial locations in the lens. We would expect this situation to produce a step change in measured resistivity at some depth below the lens surface at our theoretical x_0. We have observed such a step change at approximately $r = 0.8a$ (Fig. 8) and (*i*) conclude there is a radial dependence of intracellular resistivity; and (*ii*) therefore make the simplifying assumption that all angular dependencies can be lumped into an outer shell of thickness $0.2a$, defining this shell as the distance a (the lens radius) minus r_0.

At low frequencies the spread of current in the outer shell depends primarily on the surface membrane conductance (G_s, S/cm^2), which takes on different values in the posterior (G_p) and anterior (G_a) hemispheres:

$$G_s(\theta) = \begin{cases} G_p & 0 \le \theta \le \pi/2 \\ G_a & \pi/2 \le \theta \le \pi. \end{cases} \quad (1)$$

At high frequencies, as already pointed out, the current flow in the outer shell depends on the effective intracellular and extracellular resistivities. For later convenience, we write $R_{i,r}$ in the outer shell in terms of the average angular conductivity, $1/\bar{R}_i$, and an unknown angular conductivity function $g(\theta)$ to create an effective angular conductivity (see Eq. 2).

$$R_{i,r} = \bar{R}_i/[1 + g(\theta)] \quad r_0 \le r \le a \quad (2)$$

$$\int_0^{\pi} g(\theta) \sin\theta \, d\theta = 0. \quad (3)$$

Analytical analysis of this situation was not possible, so an additional approximation had to be made. We treat the outer shell as a semi-lumped circuit that sets boundary conditions on the voltage within the lens; we allow distributed voltage gradients in the radial direction but ignore angular currents in the thin outer shell. The equivalent circuit for one such outer shell segment is shown in Fig. 3 *B*.

Comparison of theory and data

Application of this analysis to determine the actual angular variations in $R_{i,r}$ and G_s is shown in Fig. 4. We model G_s as a step function (Fig. 4 *A*) with a value on the posterior surface G_p and on the anterior surface G_a. The values of G_p and G_a were determined by repetitively curvefitting all our angular data with different fixed values until the angular dependence was largely eliminated (Fig. 4 *A, dashed line*). The value of the effective intracellular resistivity, $\bar{R}_i/[1 + g(\theta)]$, was determined by adjusting $\bar{R}_i$ and two $g(\theta)$ related parameters G_0 and G_2 (see Appendix for mathematical description) until our model-generated high frequency voltage (Fig. 4 *B, solid line*) adequately fit our experimentally obtained high frequency data for the average voltage $\psi(r_0, \theta)$ at each θ (Fig. 4 *B, circles*). We estimate $R_{i,r}(\theta)$ at $r = r_0$ (Fig. 4 *C, smooth line*) from the radial gradient in voltage divided by the current density. Though the values of G_0 and G_2 are defined as weighted averages of $g(\theta)$, they are arbitrarily selected to generate a reasonable fit to the voltage

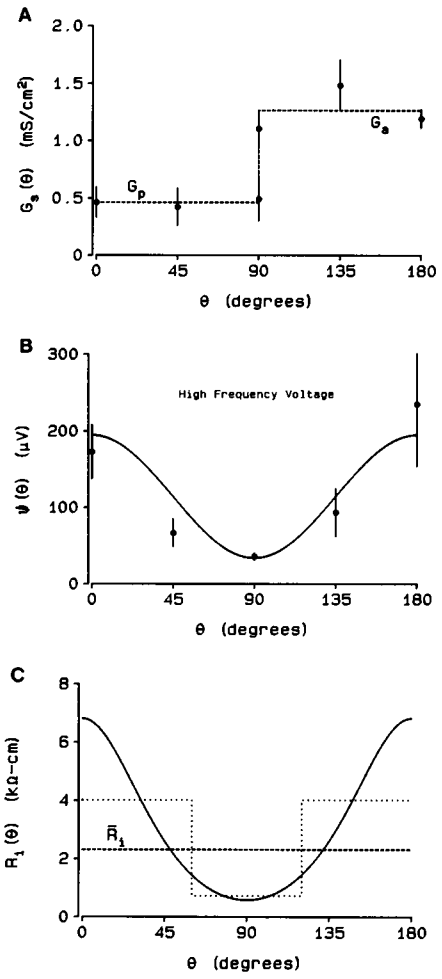

FIGURE 4 Application of angular analysis to determine G_s and $R_{i,r}$. (*A*) $G_s(\theta)$ was modeled as a step function based on the results of the old model. Final values for G_p and G_a were determined by repetitively varying them and curvefitting all data until the angular dependence of G_s was minimized. (*B*) The experimentally measured points, ±SD, are the average RMS voltage responses to an 800-Hz sinusoidal current of 1 μA RMS amplitude. $\bar{R}_i$, G_0, and G_2 were adjusted to obtain the best fit of the high frequency, theoretically calculated voltage (*solid line*) to the actual $\psi(\theta)$ (*circles*), which, given the standard deviations of the data, appeared to be modeled adequately by the angular average of the voltage plus the Legendre polynomial $P_2(\cos\theta)$. (*C*) An angular dependence was imposed on $R_{i,r}$ based on the values of the high frequency voltage determined in *B*. Note that a fourfold variation in induced voltage from pole to equator required about a 10-fold variation in resistivity.

data. Thus, they are not necessarily constrained to fit our value of $R_{i,r}(\theta)$ calculated from the ratio of voltage gradient to current density. To place some constraints on the values of G_0 and G_2, we use them to define G_{min} and G_{max} terms, which are the magnitudes of the angular averages of $g(\theta)$ between 0° and $\bar{\theta}$, and $\bar{\theta}$ and 90°, respectively. The average values of $R_{i,r}(\theta)$ on either side of $\bar{\theta}$ are shown as the dotted lines in Fig. 4 *C*, whereas the overall average $\bar{R}_i$ is shown as the dashed line. The values of G_0 and G_2 are selected so that the predicted averages G_{max} and G_{min} approximately fit the value of $R_{i,r}(\theta)$ calculated from the ratio of the voltage gradient to the current density.

The fits to the data are clearly not perfect; however, we feel that the curves in Fig. 4 *C* provide a reasonable first approximation to the angular dependence of $R_{i,r}$. Even at this crude level, we see that the roughly 4-fold variation in $\psi(r, \theta)$ requires about a 10-fold variation in $R_{i,r}$ due to the nonuniform current density: the high frequency current density is greatest where resistivity is lowest, and vice versa; hence $\psi(r_0, \theta)$ significantly underestimates the actual angular variation in resistivity.

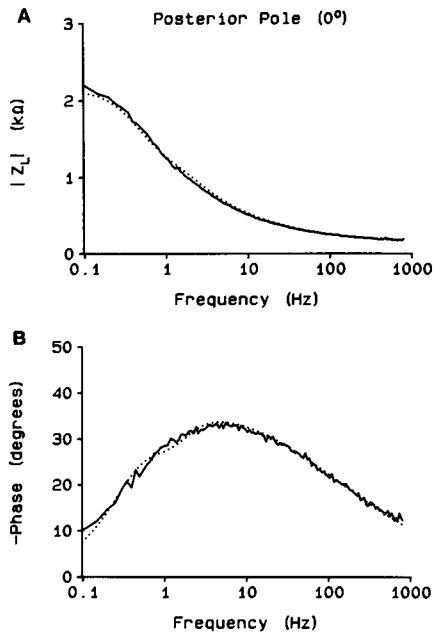

FIGURE 5 Impedance data and resulting curvefits. Both the magnitude and phase angle of the impedance are collected using the Hewlett Packard Fourier analyzer (*solid lines*) and curvefit by computer to the model shown in Fig. 1 using a least-squares method (*dotted lines*) to obtain estimates of $R_{i,r}$, $R_{e,r}$, g_m, G_s, and C_s. We assume $c_m = 1\ \mu F/cm^2$ and $S_m/V_t = 6{,}000\ cm^{-1}$. The membrane area per unit volume (S_m/V_t) is estimated from structural studies and the value of 1 $\mu F/cm^2$ was considered a physically reasonable estimate of c_m.

RESULTS

Impedance data in the frequency range of 0.08–800 Hz were collected using a 5420 Fourier analyzer. Parameter values for the equivalent circuit model (Fig. 1 *B*), normalized to the lens size, were obtained by a computerized least-squares fit. Typical impedance magnitude and phase angle data, and the associated computer fits, are shown in Fig. 5. Certain information can be obtained directly from the impedance magnitude data, without curvefitting, because of the structure of the lens and the inherent time constants involved. At high frequencies, the membrane capacitances c_m and C_s act as short circuits and Z_L (the input impedance) is simply a series resistance reflecting the value of $R_{i,r}$. $R_{i,r}$, in turn, is the sum of the cytoplasmic resistance and the gap junctional resistance connecting fiber cells. Since the cytoplasmic resistivity is small compared with $R_{i,r}$, changes in the high frequency component reflect real-time changes in gap junctional conductance. At low frequencies (near DC), Z_L is largely determined by $R_{e,r}$ and the membrane conductances g_m and G_s. Therefore, the low frequency component of the impedance magnitude reflects the reciprocal of the membrane conductance and the integrity of the cell membranes.

Angular variation of impedance

The data in Fig. 5 were recorded from the posterior pole of the lens ($\theta = 0°$); however, there is a systematic angular variation in the magnitude of the impedance moving from the posterior to the anterior (180°) pole. In general, the lens impedance at all frequencies is lowest at the equator (90°), and the high frequency component suggests that gap junctional coupling between fiber cells is greatest in this region. As explained in the theory section, the lower equatorial impedance shunts a larger fraction of injected current through this region. As a result, the values of $R_{i,r}$ and G_s obtained from curvefitting will deviate from their true values unless the equivalent circuit model includes an evaluation of the angular dependence of these two parameters (Fig. 4). Table 1 presents the means and standard deviations from 4–10 data sets for $\bar{R}_i$, $R_{e,r}$, g_m, and G_s, as determined from our angularly varying model of the lens impedance. The systematic angular variations in G_s and $R_{i,r}$ seem to be accounted for by our model; however, there remains some angular variation in g_m and $R_{e,r}$. Our data suggest that the input resistance of the lens is lowest at the equator even after subtracting the high frequency component, so the value of g_m may indeed vary with θ and be lower at the equator than at either pole. The observed variation in $R_{e,r}$ could be due to the complex matrix of fiber cell sutures present at the poles (Kuszak et al., 1992). One assumption of our model, however, is that $R_{e,r} + R_{i,r} \approx R_{e,r}$ at all θ. This assumption appears to be valid, given the parameter values we derived; however, the fit to the data in Fig. 4 *B* is barely adequate. Another explanation for the angular variation in $R_{e,r}$ should not be discounted: If the ends of

TABLE 1 **Rat lens model parameters**

	0° (posterior pole)	45°	90° (equator)	135°	180° (anterior pole)
$\bar{R}_i$ (kΩ-cm)	1.2 ± 0.3	0.8 ± 0.2	1.2 ± 0.2	1.1 ± 0.4	2.3 ± 1.9
$R_{e,r}$ (kΩ-cm)	52 ± 25.3	22 ± 9.3	18 ± 3.8	30 ± 12	55 ± 15.7
g_m (μS/cm^2)	1.6 ± 0.13	2.1 ± 0.41	2.6 ± 0.61	2.0 ± 0.44	1.2 ± 0.56
G_p (mS/cm^2)	0.59 ± 0.09	0.8 ± 0.2	0.74 ± 0.13		
G_a (mS/cm^2)			1.11 ± 0.25	1.13 ± 0.29	1.11 ± 0.21

Estimates of parameters were obtained from 4–10 lenses at each location under the following conditions: c_m fixed at 1 μF/cm^2; S_m/V_t fixed at 6,000 cm^{-1}; inner $R_{i,r}$ fixed at 4.5 kΩ-cm; $\beta_i = \beta_e = 10$. Tabulated values were determined at radial locations $r \approx 0.9a$, with an average lens radius a = 0.185 ± 0.009 cm (mean ± SD). All numbers are means ± SD.

the peripheral fiber cells are essentially devoid of gap junctions, the local value of $R_{i,r}$ near the poles may become very large, rendering the above assumption invalid. This would have the effect of making $R_{e,r}$ appear very large near either pole. Both g_m and $R_{e,r}$ enter the model calculations in a complicated way that makes it difficult to incorporate θ dependence. Hence, a more rigorous evaluation of these observations will require a significant advance in our ability to model current flow in the lens.

Uncoupling of gap junctions in 20 mM calcium

Gap junctions of frog and rat lenses may uncouple in high Ca^{2+} solutions (Jacob, 1983; Gandolfi et al., 1990; Mathias et al., 1991). We studied the effect on rat lenses by bathing them in solutions containing 20 mM Ca^{2+} (partial replacement of extracellular Na^+) and 1 μM of the Ca^{2+} ionophore A23187. One such experiment is illustrated in Fig. 6. After 6.5 h, impedance data showed an approximately twofold increase in the high frequency Z_L (Fig. 6 *A*). This was accompanied by an increase in g_m and a drop in resting potential to near 0 mV, suggesting that the integrity of the fiber cell membranes was compromised by the treatment. This deterioration of the lens was also indicated visually by a generalized opacity of the tissue. The time course of the increase in $R_{i,r}$, and therefore gap junctional uncoupling, was roughly linear during the treatment (Fig. 6 *B*). When returned to normal Tyrode's solution, the lens failed to recover either its resting potential or its clarity, even after 2 h. Similar results were obtained with four other lenses, and it was concluded that elevated calcium was not a useful means to study gap junctional uncoupling and recovery in the rat lens.

Uncoupling of gap junctions by elevated CO_2

Bathing frog lenses in Ringer's solution bubbled with 100% CO_2 lowers outer cortical lens pH from 7.0 to 6.2, and produces a 40-fold increase in $R_{i,r}$ (Mathias et al., 1991). We used 20 and 100% CO_2-bubbled Tyrode's solution to lower the pH in the rat lenses. Fig. 7 *A* shows three impedance curves recorded from the anterior pole of the same lens. Note that the two concentrations of CO_2 not only produce differential uncoupling, but also that the fiber cell membrane conductance (g_m) does not increase, as with the high calcium experiments, suggesting that the fiber cell membranes maintain their structural integrity.

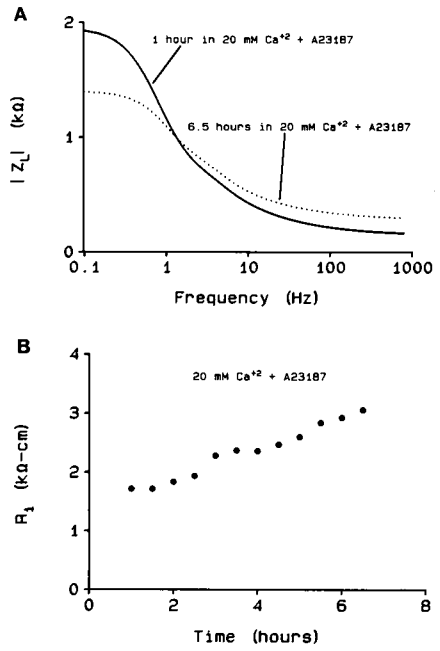

FIGURE 6 Gap junctional uncoupling in 20 mM Ca^{+2}. (*A*) After 6.5 h, the impedance magnitude shifted in a manner suggesting both decreased gap junctional coupling (increased resistance at high frequencies) and increased fiber cell membrane conductance (decreased resistance at low frequencies). (*B*) R_i increased approximately twofold during the course of the experiment, suggesting modest uncoupling of gap junctions. This was irreversible and the membrane potential remained near 0 mV after over 2 h in normal Tyrode's solution.

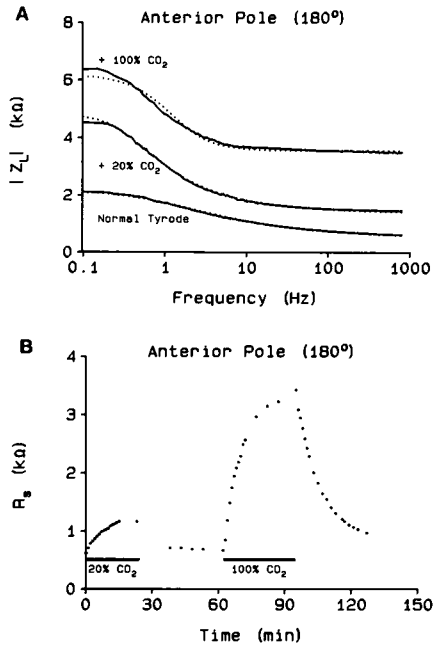

FIGURE 7 Gap junctional uncoupling in high CO_2. (*A*) Normal Tyrode's solution was bubbled with 20 and 100% CO_2 to lower lens intracellular pH. On average, 20% CO_2 produced a fivefold increase in $R_{i,r}$; 100% CO_2 produced at least a 15-fold increase since the parallel sum of $R_{i,r}$ and $R_{e,r}$ increased an average 15-fold. All three impedance curves were recorded from the anterior pole of the same lens. (*B*) Magnitude, time course, and reversibility of CO_2-induced uncoupling. Data are the high frequency series resistance (R_s) from the same lens as in *A*. The heavy bars indicate when Tyrode's bubbled with 20 or 100% CO_2 was flowing through the bath. Normal Tyrode's was flowing at all other times.

Although the membrane potential decreased during the CO_2 treatments, it recovered within 20 min after return to normal Tyrode's solution and the lens appeared healthy. Fig. 7 *B* shows the magnitude and time course of uncoupling during exposure to 20 and 100% CO_2, as well as recovery in normal Tyrode's. This was typical of all lenses studied. On average, exposure of the lens to 20% CO_2-bubbled Tyrode's produced a fivefold increase in $R_{i,r}$, whereas the 100% CO_2 caused a 15-fold increase. It should be noted we used the highest flow rates possible with our setup, ~7.5 ml/min, which is significantly slower than that used by Mathias et al. (1991) when studying frog lenses where the bath does not have to be heated.

The magnitude and time course of the CO_2-produced uncoupling shown in Fig. 7 was typical of outer fiber cells at all angular locations. We did not pursue the angular dependence of uncoupling since a proper treatment requires that the model incorporate properties of the desmosomes connecting the anterior epithelial cells. The properties of these junctions will be the subject for a later investigation.

Radial variation in pH sensitivity of gap junctions

$R_{i,r}$ varied as a step-wise function of the voltage-recording electrode depth in the lens. As the electrode was advanced inward, $R_{i,r}$ abruptly increased from ~1.2 to ~5 kΩ-cm at a depth of 0.8 of the lens radius (Fig. 8, *circles*) in normal Tyrode's. In 100% CO_2-bubbled Tyrode's (Fig. 8, *triangles*), $R_{i,r}$ measured in the outer cortical regions of the lens (>0.8) increased by a factor of 15–20; however, $R_{i,r}$ measured in the inner regions was similar to $R_{i,r}$ measured in normal Tyrode's. This suggests that the gap junctions of the inner regions (<0.8*a*) have lost their pH sensitivity and no longer uncouple at acid pH. This is consistant with the frog lenses and may be essential to normal lens function, since the pH of inner fiber cells is quite acidic (6.5–6.9; Mathias et al., 1991).

DISCUSSION

Estimates of surface cell conductance, G_s, and radial intracellular resistivity, $R_{i,r}$, obtained from curvefits to an earlier model of the lens (Mathias and Rae, 1985) indicated a consistent angular dependence, seen in G_s as a steplike increase throughout the anterior hemisphere and in $R_{i,r}$ as a smooth, symmetric fourfold pole to equator decrease in both hemispheres. We thought this variation in $R_{i,r}$ may be substantially larger than indicated (Baldo et al., 1990) for the following reason: Our determinations of lens impedance are accomplished by measuring the voltage ψ induced by injecting a known current I and using Ohm's law: $Z_L = \psi/I$. A tacit assumption is that the injected current radiates uniformly

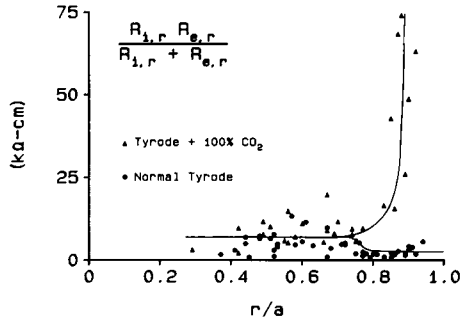

FIGURE 8 Radial variation in gap junctional conductance in normal and acidic conditions. The abscissa indicates the depth (radial location, *r*) of the voltage-recording electrode within the lens, normalized to the lens radius, *a* (0 is at the center, 1 is at the periphery). In normal Tyrode's solution (*circles*), gap junctional coupling was greatest at radial locations peripheral to $r/a = 0.8$. When bathed in 100% CO_2-bubbled Tyrode's (*triangles*), massive uncoupling was seen in the outer 20% of the lens, but the inner junctions appeared pH insensitive. Note that the solid lines are drawn by hand and simply serve to indicate the overall trends.

from the center of the lens in all directions. Clearly, the angular variations in G_s and $R_{i,r}$ will produce nonuniformities in current density and result in underestimates of the two parameters' true variance since current density will be higher where resistance is lower and vice versa. This evaluation prompted the development of the model presented here, which (*i*) incorporates the angular variation in G_s as a step function centered about the equator with a posterior hemisphere conductance G_p and an anterior hemisphere conductance G_a (Fig. 4 *A*); and (*ii*) describes the fourfold angular variation in ψ using the smoothly varying Legendre polynomial term $P_2(\cos\theta)$ such that ψ reaches its minimum at the equator (90°; Fig. 4 *B*).

The functional significance of these angular variations relates to our understanding of the physiology of the lens. The pole to pole steplike change in G_s may reflect the presence of the transporting epithelium on the anterior hemisphere, which is likely to have different ion selectivities and conductances than the fiber cells of the posterior hemisphere (Candia et al., 1970, 1971). $R_{i,r}$ is proportional to the cytoplasmic resistivity and the number of open gap junctional channels connecting cells within a small volume of the lens. Data obtained from lens homogenates show a twofold increase in resistivity going from cortical to nuclear regions (McEwan and Farnsworth, 1987); however, we confined our angular measurements of $R_{i,r}$ to the outer cortex of the lens. We therefore infer that the angular variations in $R_{i,r}$ reflect the nonuniform distribution of functional gap junctions. Our data do not allow us to decide whether the higher conductance at the equator is due to a higher density of junctions, or whether more junctions are gated open compared with the poles. Kuszak et al. (1992) provide evidence that the density of junctions is lower near the poles. Regardless, our data suggest that the equatorial gap junctional conductance is at least 10 times greater than the polar. The presence of a high equatorial conductance is probably related to the large equatorial steady-state currents reported by Robinson and Patterson (1983) and Parmelee et al. (1985). These currents may play a major role in the osmotic movement of fluid through the lens, helping to circulate nutrients and metabolites and serving to maintain the health of the inner fiber cells. The distribution of the gap junctions may direct this current.

Comparison of the estimates of rat lens parameters to those obtained from frog lens (Mathias and Rae, 1985) show some variations. The surface cell conductance is roughly double in the rat and the inner fiber cell conductance is six times greater than frog. Both the intracellular and extracellular resistivities are approximately one-third of those in frog, suggesting that gap junctional coupling may be greater in the rat, and the extracellular space is not quite as restricted (also reported by Kuszak et al., 1984). The general observation is that all resistances are somewhat lower in the mammalian lens but the relative values within the rat lens are similar to those in frog: the membrane resistance of the surface cells is much smaller than that of the fiber cells, and the effective intracellular resistivity is much smaller than extracellular resistivity. Since it is the relative values of these parameters that determine the direction of circulating fluxes, the ideas summarized in Mathias and Rae (1985) should carry over to mammalian lenses.

The response of the rat lens to high calcium was very similar to frog lens (Mathias et al., 1991). We observed an approximate doubling of $R_{i,r}$ during 6.5 h in Tyrode's containing 20 mM Ca^{2+} and the calcium ionophore A23187, accompanied by a drop in membrane potential to near 0 mV and an increase in g_m. These changes did not reverse after 2 h in normal Tyrode's, suggesting that other cellular processes in addition to gap junctional coupling had been affected. Jacob (1983) noted similar changes after a 12-h incubation in 20 mM Ca^{2+}: an approximate twofold increase in R_i and opacification of the lens. This was somewhat reversed after an additional 12-h incubation in Ca-free solution. Gandolfi et al. (1990) report a fivefold increase in R_i in rat lenses incubated for 12 h in Na-free or 10 mM Ca^{2+} Tyrode's, and a 10-fold increase after 12 h in diamide. If the exposure to elevated Ca^{2+} was terminated after 5 h, they observed partial recovery of coupling resistance and resting voltage; however, this was not complete even after 10 h in normal Tyrode's. We conclude that elevating external [Ca^{2+}] is not a useful method for studying gap junctional coupling in the intact lens.

The effects of lowered pH on the rat lens were striking in both their magnitude and reversibility. As with frog lens, we observed graded increases in impedance (i.e., decreased gap junctional conductance) when the lens was subjected to 20 and 100% CO_2-bubbled Tyrode's (Fig. 7). These changes were located in the outer 20% of the lens; at greater depths the junctions failed to uncouple (Fig. 8). Superficial uncoupling has also been observed in response to 2,4-dinitrophenol (Rae et al., 1982), which may or may not affect intracellular pH. Although we did not measure the actual pH in the presence of the CO_2, we have no reason to believe it was greatly different from that reported by Mathias et al. (1991) in frog lenses. The lack of junctional uncoupling at acid pH by the inner fiber cells is striking in both the frog and rat, and a consistency is beginning to emerge: it is likely to be essential for the inner cells to remain in contact with the more superficial outer fiber cells and the transporting epithelium capping the anterior hemisphere. This may be to allow elimination of protons and calcium from the inner cells via flux through gap junctions to the surface where ATP-driven extrusion, as well as Na/H and Na/Ca exchange, occur (Jacob, 1983;

Bassnett and Duncan, 1985; Bassnett et al., 1987; Wolosin et al., 1990).

It is interesting to note that the change in gap junctional pH sensitivity at $\sim 0.8a$ correlates with changes in fiber cell proteins. The outer cortex of the lens contains large quantities of both MIP, a 28-kD protein, and MP70, a 70-kD protein (Gruijters et al., 1987). These two proteins are thought to degrade in the outer cortex to MP22 (Takemoto and Takehana, 1986) and MP38 (Kistler and Bullivant, 1987), respectively, and may in part account for: (*1*) the three types of gap junctions found in the lens (epithelial, outer cortical, and inner cortical), and (*2*) the loss of pH sensitivity we observe at depths of $\sim 0.8a$.

APPENDIX

Partial differential equations and boundary conditions

The general equations for $\psi_{i,e}$ are simple conservation laws that require the divergence of the sum of intracellular and extracellular currents to be zero everywhere except at the center, where the current I is injected into a cell. Moreover, the divergence in extracellular current must equal the trans-membrane current.

$$\frac{1}{r^2}\frac{\partial}{\partial r}\left[\frac{r^2}{R_{i,r}}\frac{\partial \psi_i}{\partial r}+\frac{r^2}{R_{e,r}}\frac{\partial \psi_e}{\partial r}\right]+\frac{1}{r^2\sin\theta}\times\frac{\partial}{\partial\theta}\left[\frac{\sin\theta}{R_{i,a}}\frac{\partial \psi_i}{\partial\theta}+\frac{\sin\theta}{R_{e,a}}\frac{\partial \psi_e}{\partial\theta}\right]=-\frac{I\delta(r)\delta(\theta)}{2\pi r^2\sin\theta} \quad (A1)$$

$$\frac{1}{r^2}\frac{\partial}{\partial r}\left[\frac{r^2}{R_{e,r}}\frac{\partial \psi_e}{\partial r}\right]+\frac{1}{r^2\sin\theta}\frac{\partial}{\partial\theta}\left[\frac{\sin\theta}{R_{e,a}}\frac{\partial \psi_e}{\partial\theta}\right]=-\frac{S_m}{V_t}y_m(\psi_i-\psi_e). \quad (A2)$$

In the outer shell, we assume no angular current flow

$$\frac{\partial \psi_i}{\partial\theta}=\frac{\partial \psi_e}{\partial\theta}=0 \quad r_0\le r\le a \quad (A3)$$

$$-\frac{1+g(\theta)}{\bar{R}_i}\frac{\partial \psi_i(a,\theta)}{\partial r}=\begin{cases}(G_p+j\omega C_s)\psi_i(a,\theta) & 0\le\theta\le\pi/2\\ (G_a+j\omega C_s)\psi_i(a,\theta) & \pi/2\le\theta\le\pi\end{cases} \quad (A4)$$

$$\psi_e(a,\theta)=0. \quad (A5)$$

With Eqs. A3–A5, we can solve Eqs. A1 and A2 in the domain $r_0\le r\le a$ to obtain the currents $i_{i,e}(r_0,\theta)$ as functions of $\psi_{i,e}(r_0,\theta)$. These currents give boundary conditions on the normal derivative in voltage in the inner domain $0<r\le r_0$.

$$i_i(r_0,\theta)=-\frac{1}{R_i}\frac{\partial \psi_i(r_0,\theta)}{\partial r}=\left[y_{11}-\Delta G_s U\left(\theta-\frac{\pi}{2}\right)\right]\psi_i(r_0,\theta)+y_{12}\psi_e(r_0,\theta) \quad (A6)$$

$$i_e(e_0,\theta)=-\frac{1}{R_e}\frac{\partial \psi_e(r_0,\theta)}{\partial r}=y_{12}\psi_i(r_0,\theta)+y_{22}\psi_e(r_0,\theta), \quad (A7)$$

where

$$\Delta G_s=\tfrac{1}{2}(G_a-G_p) \quad (A8)$$

$$U\left(\theta-\frac{\pi}{2}\right)=\begin{cases}-1 & 0\le\theta\le\pi/2\\ +1 & \pi/2\le\theta\le\pi\end{cases}=\sum_{m=0}^{\infty}U_{2m+1}P_{2m+1}(\cos\theta)$$

$$U_{2m+1}=-\frac{(4m+3)P_{2m}(0)}{2(m+1)}. \quad (A9)$$

The parameters $y_{m,k}$ depend on the properties of the outer shell, whereas $\psi_{i,e}$ are the potentials in the inner sphere. The effective intracellular resistivity of the outer shell, $\bar{R}_i/[1+g(\theta)]$, enters the boundary conditions at r_0 in two ways. One component of each $y_{m,k}$ depends on the membranes and thus varies with frequency. This component depends only on the sum $R_e+\bar{R}_i/[1+g(\theta)]$. Since $R_e\gg\bar{R}_i$, the angular variation in $R_{i,r}$ has little consequence, so we assume

$$R_e+\bar{R}_i/[1+g(\theta)]\approx R_e+\bar{R}_i. \quad (A10)$$

The physical basis of this assumption is that at low frequencies, voltage drops in the intracellular space are small in comparison to the voltage drops across membranes. $R_{i,r}$ enters the problem only through the propagation coefficient, $\bar{\gamma}$ (cm^{-1}), for spatial gradients in the extracellular voltage, and in this role it enters in sum with $R_{e,r}$. This result is exactly analogous to our "order zero" solution in the perturbation expansion derived in Eisenberg et al. (1979) or Mathias et al. (1981).

At high frequencies, the spatially constant component of ψ_i goes to zero and the series resistance term (Mathias et al., 1991) becomes the dominant term in the solution. The series resistance varies as $R_{i,r}R_{e,r}/(R_{i,r}+R_{e,r})$, so inasmuch as $R_{e,r}\gg R_{i,r}$, this term is directly proportional to $R_{i,r}$.

Low frequency boundary conditions

We first solve for each $y_{m,k}$ that describes the membrane determined component of admittance (see Eqs. A11–A13 below). These expressions omit a component of y_{22} that scales with $(a-r_0)\bar{R}_i/[1+g(\theta)]$. This component is subsequently added to the solution for $\psi_{i,e}$ in the inner sphere by solving for the high frequency limit. The dominant low frequency terms are

$$y_{11}\approx-\bar{y}_e(r_0)-\left[2-\frac{r_0\sinh\bar{\gamma}_a}{a\sinh\bar{\gamma}r_0}-\frac{a\sinh\bar{\gamma}r_0}{r_0\sinh\bar{\gamma}a}\right]\frac{a}{r_0}\Delta\bar{y}+\frac{a^2}{r_0^2}[\bar{y}_e(a)+\bar{y}_s] \quad (A11)$$

$$y_{12}\approx\bar{y}_e(r_0)+\left[1-\frac{r_0\sinh\bar{\gamma}a}{a\sinh\bar{\gamma}r_0}\right]\frac{a}{r_0}\Delta\bar{y} \quad (A12)$$

$$y_{22}\approx-\bar{y}_e(r_0)+\frac{\sinh\bar{\gamma}a}{\sinh\bar{\gamma}r_0}\Delta\bar{y}, \quad (A13)$$

where

$$\bar{y}_s=\tfrac{1}{2}(G_a+G_p)+j\omega C_s \quad (A14)$$

$$\bar{\gamma}^2=(\bar{R}_i+R_e)\frac{S_m}{V_t}y_m \quad (A15)$$

$$\bar{y}_e(r) = \frac{\bar{\gamma}}{\bar{R}_i + R_e}\left(\coth \bar{\gamma} r - \frac{1}{\bar{\gamma} r}\right) \quad \text{(A16)}$$

$$\Delta\bar{y} = \frac{\bar{\gamma}}{(\bar{R}_i + R_e)\sinh \bar{\gamma}(a - r_0)}. \quad \text{(A17)}$$

As one can see, the angular dependence of the boundary conditions in Eqs. A6 and A7 is due to the angular variation in G_s.

High frequency boundary conditions

At high frequencies

$$\psi_i \to \psi_e = IR_s(r, \theta), \quad j\omega \to \infty \quad \text{(A18)}$$

$$\left[\frac{1}{R_{i,r}} + \frac{1}{R_{e,r}}\right]\frac{1}{r^2}\frac{\partial}{\partial r}\left[r^2\frac{\partial R_s}{\partial r}\right] + \left[\frac{1}{R_{i,a}} + \frac{1}{R_{e,a}}\right]\frac{1}{r^2\sin\theta}\frac{\partial}{\partial\theta}\left[\sin\theta\frac{\partial R_s}{\partial\theta}\right] = -\frac{\delta(r)\delta(\theta)}{2\pi r^2\sin\theta}$$
$$j\omega \to \infty. \quad \text{(A19)}$$

We solve Eq. A19 in $r_0 \le r \le a$ with the condition $R_s(a, \theta) = 0$ and find that the boundary condition at r_0 is

$$-\left[\frac{1}{R_i} + \frac{1}{R_e}\right]\frac{\partial R_s(r_0, \theta)}{\partial r} = \left[\frac{1 + g(\theta)}{\bar{R}_i} + \frac{1}{R_e}\right]\frac{a/r_0}{a - r_0}R_s(r_0, \theta) \quad j\omega \to \infty. \quad \text{(A20)}$$

The angular dependence of this component is due to the angular variation of $R_{i,r}$ in the outer shell.

Solutions

The solution to Eqs. A1 and A2 in $0 < r \le r_0$, with the boundary conditions in Eqs. A6 and A7, is found using the perturbation approach described in Eisenberg et al. (1979), and standard techniques for expanding in a series of Legendre polynomials, $P_m(\cos\theta)$ (e.g., Jackson, 1975, chapter 3). The solution contains a term that is part of R_s, namely, the angular average of the high frequency voltage drop between r and r_0:

$$\frac{R_i}{4\pi}\left[\frac{1}{r} - \frac{1}{r_0}\right].$$

This term also appears in the general expression for R_s determined by solving Eq. A19 in $0 \le r \le r_0$ with the boundary condition of Eq. A20; hence, we take the union of the two solutions as our complete solution in Eq. A21 below. The intracellular voltage is $\psi_i(r, \theta, j\omega) = I(j\omega) \times Z_L(r, \theta, j\omega)$, where

$$Z_L(r, \theta, j\omega) = Z_0(j\omega) + Z_0(j\omega)R_i r_0\Delta G_s[S(r, \theta) + Z_0(j\omega)4\pi r_0^2\Delta G_s S_0] + R_s(r, \theta) - \epsilon[Z_e(r) + Z_e(0)] \quad \text{(A21)}$$

and

$$Z_0(j\omega) = \frac{1}{4\pi r_0^2\{y_{11} + 2y_{12} + y_{22} - (y_{22} + y_{12})^2/[y_{22} + y_e(r_0)]\}} \quad \text{(A22)}$$

$$y_e(r) = \frac{\gamma}{R_i + R_e}\left(\coth \gamma r - \frac{1}{\gamma r}\right) \quad \text{(A23)}$$

$$\gamma^2 = (R_i + R_e)\frac{S_m}{V_t}y_m \quad \text{(A24)}$$

$$S(r, \theta) = \sum_{n=0}^{\infty}\frac{U_{2n+1}}{q_{2n+1}}\left[\frac{r}{r_0}\right]^{q_{2n+1}}P_{2n+1}(\cos\theta) \quad \text{(A25)}$$

$$q_{2n+1} = \tfrac{1}{2}[\sqrt{1 + 8\beta_i(2n + 1)(n + 1)} - 1] \quad \text{(A26)}$$

$$S_0 = \sum_{n=0}^{\infty}\frac{(U_{2n+1})^2}{(4n + 3)q_{2n+1}} \quad \text{(A27)}$$

$$Z_e(r) = Z_0(j\omega)\left[1 - \frac{y_{22} + y_{12}}{y_{22} + y_e(r_0)}\frac{r_0\sinh\gamma r}{r\sinh\gamma r_0}\right] \quad \text{(A28)}$$

$$\epsilon = \frac{R_i}{R_i + R_e}. \quad \text{(A29)}$$

The angular dependence to the high frequency voltage is, to the accuracy of our data, sufficiently described by terminating its Legendre series at $P_2(\cos\theta)$. Hence,

$$R_s(r, \theta) \simeq \frac{R_i R_e}{R_i + R_e}\frac{1}{4\pi}\left[\frac{1}{r} - \frac{1}{r_0}\right] + \frac{\bar{R}_i R_e}{\bar{R}_i + R_e}\frac{1}{4\pi}\left[\frac{1}{r_0} - \frac{1}{a}\right] + \frac{5G_0}{1 + G_2 + \frac{a - r_0}{\alpha a}p - G_0^2}\frac{\bar{R}_i R_e}{\bar{R}_i + R_e}\frac{1}{4\pi} \times \left[\frac{1}{r_0} - \frac{1}{a}\right]\left[G_0 - \left(\frac{r}{r_0}\right)^p P_2(\cos\theta)\right], \quad \text{(A30)}$$

where

$$G_0 = \frac{R_e}{\bar{R}_i + R_e}\frac{1}{2}\int_0^{\pi} g(\theta)P_2(\cos\theta)\sin\theta\, d\theta \quad \text{(A31)}$$

$$G_2 = \frac{R_e}{\bar{R}_i + R_e}\frac{5}{2}\int_0^{\pi} g(\theta)[P_2(\cos\theta)]^2\sin\theta\, d\theta \quad \text{(A32)}$$

$$\alpha = \left[\frac{1}{\bar{R}_i} + \frac{1}{R_e}\right]\Big/\left[\frac{1}{R_i} + \frac{1}{R_e}\right] \simeq \frac{R_i}{\bar{R}_i} \quad \text{(A33)}$$

$$p = \tfrac{1}{2}[\sqrt{1 + 24\beta} - 1] \quad \text{(A34)}$$

$$\beta = \left[\frac{\beta_i}{R_i} + \frac{\beta_e}{R_e}\right]\Big/\left[\frac{1}{R_i} + \frac{1}{R_e}\right] \simeq \beta_i. \quad \text{(A35)}$$

Analysis of data

Fig. 4 shows the results of this analysis applied to determine the actual angular variation in $R_{i,r}$ and G_s. The voltage data in Fig. 4 *B* have significant variance and we found that the angular variation, $g(\theta)$, was not uniquely determined by these data alone. However, we have additional information about $g(\theta)$ through the values of G_0 and G_2 (Eqs. A31 and A32). The average of $g(\theta)$ over $0 \le \bar{\theta}$ and $\theta > \bar{\theta}$, where by definition $g(\bar{\theta}) = 0$, is given by

$$G_{min} = \frac{1}{1 - \cos\bar{\theta}}\int_0^{\bar{\theta}} g(\theta)\sin\theta\, d\theta \quad \text{(A36)}$$

and

$$G_{max} = \frac{1}{\cos\bar{\theta}}\int_{\bar{\theta}}^{\pi/2} g(\theta)\sin\theta\, d\theta. \quad \text{(A37)}$$

Given that the angular average of $g(\theta)$ is zero, for equal areas between $(0, \bar{\theta})$ and $(\bar{\theta}, \pi/2)$ we require

$$1 - \cos\bar{\theta} = \frac{G_{max}}{G_{max} + G_{min}}. \quad \text{(A38)}$$

The integrals in Eqs. A36 and A37 are related to G_0 and G_2 by

$$G_0 = -\frac{G_{max}}{2}(1 + \cos\bar{\theta})\cos\bar{\theta} \qquad (A39)$$

$$G_2 = \frac{9}{4}G_{min}(1 - \cos^2\bar{\theta})\left(\frac{1}{9} - \cos^2\bar{\theta}\right). \qquad (A40)$$

We solved Eqs. A38–A40 for G_{min} and G_{max} and in Fig. 4 *C* we have graphed the predicted averages (straight lines) on top of the derived function $g(\theta)$. By constraining G_0 and G_2 to produce values of G_{min} and G_{max} that approximately describe $g(\theta)$, we were able to determine the angular dependence of $R_{i,r}(\theta)$ shown in Fig. 4 *C*.

This work was supported by NIH grant EY-06391.

Received for publication 19 November 1991 and in final form 30 March 1992.

REFERENCES

Baldo, G. J., R. T. Mathias, and T. Hagstrom. 1990. Gap junctional coupling in the rat lens. *Invest. Ophthalmol. Visual Sci.* 31:336*a*. (Abstr.)

Bassnett, S., and G. Duncan. 1985. Direct measurement of pH in the rat lens by ionsensitive microelectrodes. *Exp. Eye Res.* 40:585–590.

Bassnett, S., P. C. Croghan, and G. Duncan. 1987. Diffusion of lactate and its role in determining intracellular pH in the lens of the eye. *Exp. Eye Res.* 44:143–147.

Candia, O. A., P. J. Bentley, and C. D. Mills. 1970. Short-circuit current and active Na transport across isolated lens of the toad. *Am. J. Physiol.* 220:558–564.

Candia, O. A., P. J. Bentley, C. D. Mills, and H. Toyofuku. 1971. Assymetrical distribution of the potential difference in toad lens. *Nature (Lond.)*. 227:852–853.

Eisenberg, R. S., V. Barcilon, and R. T. Mathias. 1979. Electrical properties of spherical syncytia. *Biophys. J.* 25:151–181.

Gandolfi, S. A., G. Duncan, J. Tomlinson, and G. Maraini. 1990. Mammalian lens inter-fiber resistance is modulated by calcium and calmodulin. *Curr. Eye Res.* 9:533–541.

Gruijters, W. T. M., J. Kistler, S. Bullivant, and D. A. Goodenough. 1987. Immunolocalization of MP70 in lens fiber 16–17 nm intercellular junctions. *J. Cell Biol.* 104:565–572.

Jackson, J. D. 1975. Classical Electrodynamics. John Wiley & Sons, Inc., New York.

Jacob, T. J. C. 1983. Raised intracellular free calcium within the lens causes opacification and cellular uncoupling in the frog. *J. Physiol. (Lond.)*. 341:595–601.

Kistler, J., and S. Bullivant. 1987. Protein processing in lens intercellular junctions: cleavage of MP70 into MP38. *Invest. Ophthalmol Visual Sci.* 28:1687–1692.

Kuszak, J. R., Y. H. Shek, K. C. Carney, and J. L. Rae. 1984. Comparative analysis of crystalline lens gap junctions. *In* Proceedings of the 42nd Annual Meeting of the Electron Microscopy Society of America. G. W. Bailey, editor. San Francisco Press Inc., San Francisco, CA. 114–117.

Kuszak, J. R., K. L. Peterson, and H. G. Brown. 1992. Electron microscopic observations of the crystalline lens. *In* Electron Microscopy of the Visual System: The Anterior Segment of the Eye. Special issue of *J. Electron Microsc. Tech.* In press.

Mathias, R. T., and J. L. Rae. 1985. Transport properties of the lens. *Am. J. Physiol.* 249:C181–C190.

Mathias, R. T., and J. L. Rae. 1989. Cell to cell communication in lens. *In* Cell Interactions and Gap Junctions. Vol. I. N. Sperelakis and W. C. Cole, editors. CRC Press, Inc., Boca Raton, FL. 30–47.

Mathias, R. T., J. L. Rae, and R. S. Eisenberg. 1979. Electrical properties of structural components of the crystalline lens. *Biophys. J.* 25:181–201.

Mathias, R. T., J. L. Rae, and R. S. Eisenberg. 1981. The lens as a non-uniform spherical syncytium. *Biophys. J.* 34:61–83.

Mathias, R. T., G. Riquelme, and J. L. Rae. 1991. Cell to cell communication and pH in the frog lens. *J. Gen. Physiol.* 98:1085–1103.

McEwan, J. R., and P. N. Farnsworth. 1987. Regional resistivity variations in lens homogenates. *Exp. Eye Res.* 44:567–576.

Parmelee, J. T., K. R. Robinson, and J. W. Patterson. 1985. Effects of calcium on the steady outward currents at the equator of the rat lens. *Invest. Ophthalmol. & Visual Sci.* 26:1343–1348.

Rae, J. L., R. D. Thomson, and R. S. Eisenberg. 1982. The effect of 2-4 dinitrophenol on cell to cell communication in the frog lens. *Exp. Eye Res.* 35:597–609.

Robinson, K. R., and J. W. Patterson. 1983. Localization of steady currents in the lens. *Curr. Eye Res.* 2:843–847.

Takemoto, L., and M. Takehana. 1986. Covalent change of major intrinsic polypeptide (MIP26K) of lens membrane during human senile cataractogenesis. *Biochem. Biophys. Res. Commun.* 135:965–971.

Wolosin, J., L. Alvarez, and O. Candia. 1990. HCO_3^- transport in the toad lens epithelium is mediated by electronegative Na^+-dependent symport. *Am. J. Physiol.* 258:C855–C861.